NANOSYSTEMS:
PHYSICS, CHEMISTRY, MATHEMATICS

Original article

Lukashenko S.Yu., et al. *Nanosystems: Phys. Chem. Math.*, 2025, **16** (6), 770–777.
http://nanojournal.ifmo.ru
DOI 10.17586/2220-8054-2025-16-6-770-777

Effect of nanoscale water media confinement on the approach curve in SICM

Stanislav Yu. Lukashenko[a], Olga M. Gorbenko[b], Mikhail L. Felshtyn[c], Ivan D. Sapozhnikov[d], Stepan V. Pichakhchi[e], Mikhail V. Zhukov[f], Alexander O. Golubok[g]

Institute for Analytical Instrumentation of the Russian Academy of Sciences, Russia

[a]lukashenko13@mail.ru, [b]gorolga64@gmail.com, [c]mfelsztyn@yandex.ru, [d]isapojnikov@gmail.com, [e]pichakhchi.s@yandex.ru, [f]cloudjyk@yandex.ru, [g]aogolubok@mail.ru

Corresponding author: S. Yu. Lukashenko, lukashenko13@mail.ru

ABSTRACT The features of the ion current dependence on distance when a glass nanopipette with an aperture diameter of ∼100 nm approaches the surface of a solid dielectric in a scanning ion conductivity microscope have been studied. A characteristic peak in the approach curve has been observed when the electrode in the nanopipette with an electrolyte is negatively biased relative to electrode in the bath, while a monotonic current decline occurs with a positive bias. To explain this unusual behavior of the ion current, the model accounting for the overlap of electric double layers and water confinement phenomenon in nanochannels and nanogaps have been proposed. The model demonstrates good agreement with the experimental data and provides a basis for quantitative assessment of surface charge at electrolyte–solid interfaces with nanometer-scale spatial sensitivity.

KEYWORDS nanoscale water confinement, nanopore, peak-effect, Poisson–Nernst–Planck equations, surface charge density

ACKNOWLEDGEMENTS This work is supported by the Ministry of Science and Higher Education of the Russian Federation (Project No. 075-00444-25-00, dated 26.12.2024) and by the Russian Science Foundation (Project No. 24-79-00169.

FOR CITATION Lukashenko S.Yu., Gorbenko O.M., Felshtyn M.L., Sapozhnikov I.D., Pichakhchi S.V., Zhukov M.V., Golubok A.O. Effect of nanoscale water media confinement on the approach curve in SICM. *Nanosystems: Phys. Chem. Math.*, 2025, **16** (6), 770–777.

1. Introduction

Scanning ion conductance microscopy (SICM) is a unique probe microscopy technique [1] that enables non-contact imaging of the topography and local biophysical properties of living cells and soft biological objects in physiological environments with nanometer spatial resolution [2, 3]. High-resolution studies of biological systems are also performed using atomic force microscopy (AFM) [4, 5] or advanced optical microscopy techniques that overcome the diffraction limit [6]. However, SICM has several advantages: it avoids the mechanical damage associated with AFM when probing soft samples, and it is simpler than optical approaches, which require specific fluorescent labels and specialized optical systems. Moreover, SICM inherently relies on ionic currents in liquid media – the very processes that govern cellular function. Thanks to its high spatial and functional sensitivity, SICM has become a powerful tool in cell and molecular biology, enabling studies of ion channel activity, microvilli distribution, cytoskeletal and membrane stiffness, and other critical surface properties in real time [7–9].

The principle of SICM is based on measuring the ionic current flowing between a sample and a nanopipette probe with an aperture diameter of ∼100 nm during mechanical scanning. Far from the sample surface, at distances much larger than the nanopore size, the nanopipette exhibits a saturation current (I_{sat}) that does not depend on the probe-sample separation. The conventional explanation for current reduction near the surface is the geometrical blockage of the nanopore by the sample. To maintain a nanometer-scale gap between the pipette and the surface, SICM employs a feedback control system. Thus, the dependence of ionic current on distance underlies the imaging principle of SICM. Several operating modes exist: constant-current mode [1], AC modulation modes with voltage or distance modulation [10], and the hopping mode [11], in which the probe is sequentially approached and retracted at each scanning point.

For imaging samples with pronounced surface relief, the hopping mode provides superior image quality, though at the expense of slower acquisition compared to DC or AC modes, which are effective only for relatively flat surfaces [12]. Typically, stable SICM operation is achieved by choosing a set-point current of $\sim 99 - 99.5$ % of I_{sat} [1], corresponding to approximately (0.5 – 2) nA at applied voltages of 0.1 – 1 V and noise levels of 1 – 10 pA. When using glass nanopipettes in aqueous solutions, electrical double layers (EDLs) form at the pipette surface. For apertures less than 100 nm, these EDLs overlap inside the nanopore, giving rise to nonlinear current-voltage (I–V) characteristics, known as *ion current*

© Lukashenko S.Yu., Gorbenko O.M., Felshtyn M.L., Sapozhnikov I.D., Pichakhchi S.V., Zhukov M.V., Golubok A.O., 2025

rectification (ICR). This rectification is highly sensitive to volumetric charge and has been used, for example, in pH sensing [13].

A similar phenomenon occurs when the nanopipette approaches a charged interface: the ionic current near the sample surface increases beyond the reduction expected from simple geometric blockage. This effect is referred to as *surface-induced rectification* [12]. The growing branch of $I(z)$ in this case has been theoretically analyzed in detail [14]. However, several studies [15, 16] reported an experimental peak in $I(z)$, that is, an increase in current to a maximum followed by a monotonic decay. Reanalysis of $I(V)$ data at different probe-sample distances in [17] also revealed a characteristic peak when plotted as $I(z)$. The origin of this peak remains debated: some authors [15] attributed it to "electroosmotic flow separation", but this explanation lacked quantitative support and was later shown to be negligible [18]. Notably, existing theoretical models capture only the monotonic growth of $I(z)$ with surface charge and distance, and fail to reproduce the experimentally observed descending branch. Conventional reasoning attributes this decrease solely to nanopore blockage by the sample. Yet, our experiments indicate that current reduction begins at surprisingly large probe–sample separations, and our PNP-NS simulations reveal that current enhancement due to surface charge can outweigh the geometric blockage.

Thus, the physical origin of the extremum in the SICM approach curve $I(z)$ remains unresolved. We refer to this phenomenon as the "peak effect," which is of interest from both a fundamental and applied perspective. On the one hand, studying the peak effect provides new insight into ionic transport mechanisms in microfluidic systems under nanoscale water confinement. On the other hand, the existence of such extrema must be considered in practice, since peaks in $I(z)$ can compromise the stability of SICM feedback control. At the same time, the peak effect can also be exploited for quantitative measurements, for instance, in probing surface charge densities at liquid–solid interfaces with SICM.

The aim of this work is to investigate the SICM peak effect experimentally and to develop an adequate theoretical model that incorporates the influence of nanoscale water confinement.

2. Experiment

Experimental measurements were performed using a custom-built SICM setup. Nanocapillaries were fabricated from borosilicate glass capillaries BF-100-69 (Shutter Instruments, USA) using a PMP-107 puller (Micro Data Instruments, Inc., USA) by the method of thermal pulling and breaking of glass microcapillaries with outer and inner diameters of 1.2 and 0.69 mm, respectively. The characterization procedure for nanopipettes has been described elsewhere [19]. The cone angle of the nanocapillary tip was about 3°, and the nanopore diameter at the apex was approximately 100 nm. The average ion current rectification (ICR) factor was about 1.15. Approach curves were measured on polystyrene and on cover glass substrates etched in a 10 % NaOH solution at 250 °C. Samples were fixed at the bottom of a Petri dish filled with 1× PBS, the same electrolyte used to fill the nanopipettes. Ag/AgCl electrodes were prepared from 300 μm silver wires chloritized according to [20]. A potential bias from 0 to $\pm$1 V was applied to the electrode inside the glass nanopipette. To minimize mechanical vibrations, acoustic noise, and electromagnetic interference, the setup was mounted on an active vibration-isolation table and enclosed within a Faraday cage. A schematic of the experimental setup is shown in Fig. 1.

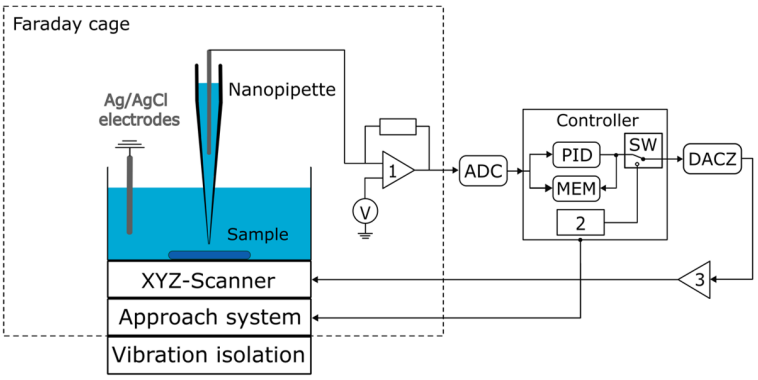

FIG. 1. Schematic diagram of the SICM experimental setup. 1 – current-to-voltage converter, 2 – signals generator, 3 – high-voltage amplifier

For each sample, the ionic current was recorded as a function of the pipette-sample separation at randomly selected surface points. At positive potentials applied to the nanopipette electrode, the approach curves $I(z)$ showed a monotonic decrease in current upon approaching the surface. A representative example measured on etched cover glass is shown in Fig. 2(a), and for polystyrene in Fig. 3(a, curve 1).

In contrast, at negative pipette biases, the $I(z)$ curves exhibited a pronounced peak, as illustrated in Fig. 2(b) and Fig. 3(b, curve 1). SICM images of the same etched glass region, acquired in hopping mode at opposite bias polarities, are shown in Fig. 2(c) and Fig. 2(d). The set-point currents used for imaging are indicated by circles on the $I(z)$ curves.

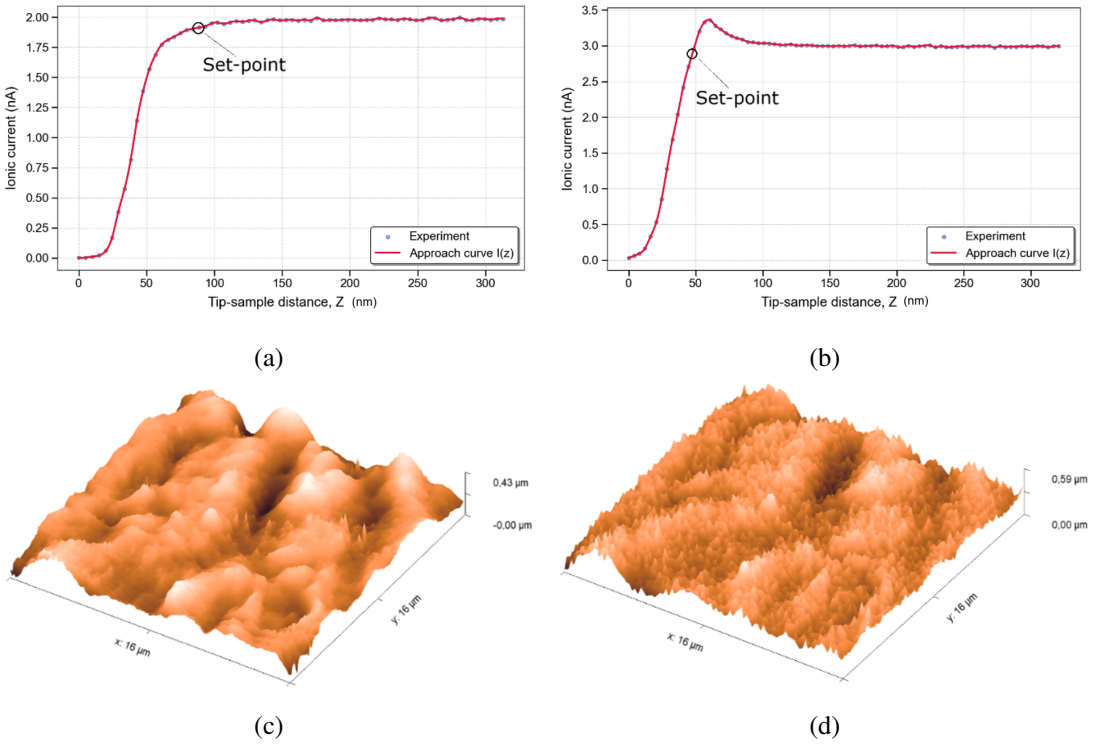

FIG. 2. Approach curves and SICM images for NaOH-etched cover glass. (a, b) $I(z)$ curves at $+300$ mV and -300 mV pipette potentials; (c, d) SICM images of the same sample fragment obtained at positive and negative pipette biases, respectively

Notably, in the case of polystyrene, approach curves with peaks were observed in ∼60 % of randomly selected surface locations, whereas for etched glass, the peak effect was consistently observed at all locations. The peak heights also varied across different positions on the same sample. Importantly, no peaks were ever observed at positive pipette biases. We refer to the emergence of a peak in the $I(z)$ dependence upon approaching the sample surface as the "peak effect."

3. Modeling

To calculate the approach curves $I(z)$ while accounting for the nanopipette geometry, we developed a two-dimensional axisymmetric mathematical model in *COMSOL Multiphysics*, using parameters consistent with our experiments (see in Supplementary materials). For comparison with experimental data, we employed both the standard Poisson–Nernst–Planck–Navier–Stokes (PNP-NS) framework commonly used to describe ionic currents in SICM [19, 21–23] and a modified version proposed here, which incorporates variations of dielectric permittivity, diffusion coefficients, and viscosity under nanoscale water confinement. For reference, we also compared our results with calculations based on the orthodox Ohmic theory [24].

3.1. Standard Poisson–Nernst–Planck–Navier–Stokes model

The ionic flux N_i in micro- and nanofluidic systems is typically described by the PNP-NS system [19, 21–23]:

$$N_i = -D_i \nabla C_i - z_i F u_i C_i \nabla \Phi + u c_i, \tag{1}$$

where D_i is the diffusion coefficient, u_i is the ion mobility, z_i is the ionic charge, F is the Faraday constant, Φ is the electric potential, u is the velocity vector, C_i is the concentration of specific ions type. The first term corresponds to diffusion driven by concentration gradients, the second – to electrophoresis driven by electric field gradients, and the third – to convection through electrolyte flow. In the standard model, diffusion coefficients and ion mobilities are treated as constant throughout the computational domain. For Na^+ and Cl^-, diffusion coefficients were taken from [25], and ion mobilities were calculated using the Nernst–Einstein relation:

$$\mu = \frac{D}{k_B T}, \tag{2}$$

where R is the gas constant and T is the absolute temperature. The surface charge density σ in the electrical double layer (EDL) was defined as:

$$\sigma = -\sqrt{8\varepsilon\varepsilon_0 c_0 k_B T} \cdot \sinh\left(\frac{ze\varphi_0}{2k_B T}\right), \tag{3}$$

where ε is the dielectric constant of the medium, ε_0 is the vacuum permittivity, k_B is the Boltzmann constant, T is the temperature, φ_0 is the surface potential, z is the valency of surface bonds, e is the elementary charge.

To compute the electrostatic field distribution in the EDL, the condition of electroneutrality was not imposed. Instead, the Poisson equation with volumetric charge density was used:

$$\nabla^2\Phi = -\frac{F}{\varepsilon\varepsilon_0}\sum_i z_i c_i, \tag{4}$$

where z_i is the ionic charge, c_i is the concentration of ions of a specific sign.

The third term in equation (1) accounts for electroosmotic flow (EOF), which arises in the diffuse layer. The EOF velocity was found by solving the Helmholtz–Smoluchowski equation:

$$u_{\text{EOF}} = \frac{\zeta\varepsilon\varepsilon_0}{\mu}\nabla\Phi, \tag{5}$$

where Φ is the electric potential, ζ is the zeta potential of the surface.

The EOF velocity in the computational domain was found using the Navier–Stokes equation (Laminar Flow solver):

$$\rho\,(\vec{u}\cdot\nabla)\,\vec{u} = \mu\Delta\vec{u} - \nabla p, \tag{6}$$

where ρ is the electrolyte density, $\vec{u}$ is the flow velocity, p is the pressure, μ is the kinematic viscosity.

Figure 3(a, dashed curve 3) and Fig. 3(b, dashed curve 3) show the calculated $I(z)$ curves obtained using the standard PNP-NS model equations (1–6) for positive and negative pipette biases, respectively. In these simulations, dielectric permittivity, diffusion coefficients, viscosity, and ion mobilities were assumed uniform throughout the domain. For comparison, the orthodox Ohmic approach based on resistance [24] is also shown (Fig. 3, dashed curves 4). Numerical values of simulation parameters are listed in Supplementary materials.

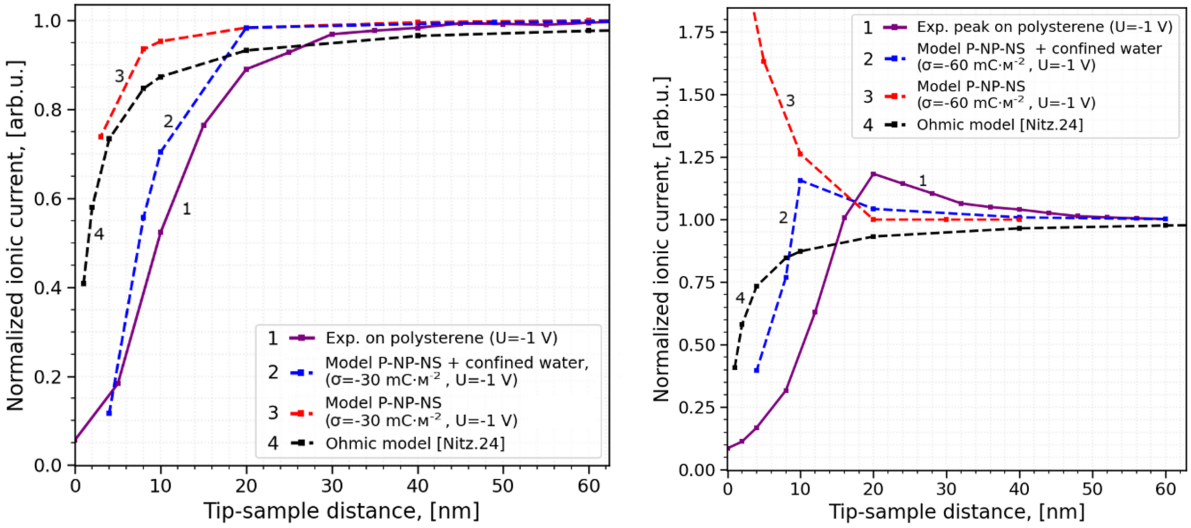

(a) (b)

FIG. 3. Comparison of experimental approach curves $I(z)$ with theoretical curves calculated using different models. (a) Positive bias applied to the nanopipette electrode. (b) Negative bias applied to the nanopipette electrode. PNP-NS models account for sample surface charge density σ. NP's surface charge density for all modeled cases was $\sigma_{pip} = -30$ mC·m^{-2}

3.2. Modified Poisson–Nernst–Planck–Navier–Stokes model under nanoscale water confinement

The standard PNP-NS model described above does not account for interionic interactions or for the changes in physicochemical properties of electrolytes that arise under nanoscale confinement of water. It is well established that water near solid interfaces exhibits properties markedly different from those of bulk water. Molecules form structured interfacial layers with restricted mobility, giving rise to two coupled effects: an increase in viscosity and a decrease in dielectric permittivity.

For instance, it has been reported that in 40 nm gaps, water viscosity is reduced by 5 % compared to bulk values, while at 1 nm separations it increases by nearly an order of magnitude [26–28]. Molecular dynamics simulations [29] further show that when two surfaces are separated by > 100 nm, water retains bulk-like properties with dielectric permittivity $\varepsilon \approx 80$. As the gap decreases, however, ε drops by an order of magnitude to values as low as 5 – 10. This finding has also been confirmed experimentally [30].

A reduction in ε lowers the electrostatic screening of ions by water, thereby strengthening ion–ion interactions according to Debye–Hückel theory. In the extended Debye–Hückel–Onsager approximation, the ionic activity coefficient γ_i is explicitly linked to dielectric permittivity [31]:

$$\log_{10}\gamma_i = -\frac{Az^2\sqrt{C_i}}{1+Ba\sqrt{C_i}}, \tag{7}$$

where

$$A = \frac{e^2 B}{2.303 \cdot 8\pi\varepsilon_0\varepsilon k_B T}, \tag{8}$$

$$B = \sqrt{\frac{2e^2 N_A}{\varepsilon_0\varepsilon k_B T}}. \tag{9}$$

Here a is the effective ionic radius, C_i is the molar concentration.

The drop in ε increases the constant A, leading to a reduction in the activity coefficient γ. Under these conditions, bulk diffusion coefficients can no longer be applied. First, tabulated diffusion coefficients are given for infinite dilution, and second, they assume bulk water with $\varepsilon \approx 80$. At electrolyte concentrations above 10 mM/L, ion–ion interactions become significant [32]. A thermodynamic description of diffusion accounting for ion activity, originally developed by Lewis, Debye, and Onsager [31–33], introduces a correction to the diffusion coefficient:

$$D_i = D_i^0\left(1 + C_i \cdot \frac{\delta \ln\gamma_i}{\delta C_i}\right), \tag{10}$$

where D_i^0 is the diffusion coefficient at infinite dilution, C_i is the electrolyte concentration, γ_i is the ionic activity coefficient.

Our simulations show that under *surface-induced rectification* at surface charge densities of -30 mC/m^2, the local ion concentration in the gap can increase 2–3 fold relative to bulk (150 mM/L), while the corrected diffusion coefficient (eq. (10)) decreases by $\sim$10 %.

The dependence $D(\varepsilon)$ calculated from equations (7–10) is shown in Fig. 4. We found that the diffusion coefficient (eq. (10)) is more dependent on the dielectric constant than on the concentration. For example, at a gap of $\sim$15 nm, $\varepsilon \approx 30$, corresponds to a $\sim$20 % reduction in the diffusion coefficient according to the Lewis–Debye–Onsager model [31]. As reported in [30] with a further decrease of the gap, the permittivity will continue to decrease even more. With the dielectric permittivity value of $\varepsilon \approx 7$, the coefficient of diffusion of the aqueous solution with a concentration of $C = 150$ mM/L via equation (10) tends to zero (Fig. 4).

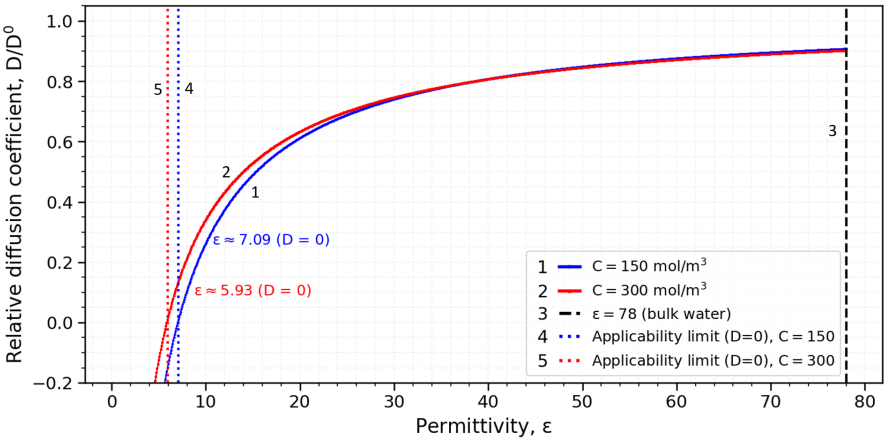

FIG. 4. The dependence of the diffusion coefficient on the electrolyte permittivity in the water confinement conditions

This means that with such low values of dielectric permeability, equation (10) ceases to work for the water media. It is clear that $\varepsilon \approx 7$ is a critical value for the dielectric permeability of an aqueous solution of electrolyte, below which there is a radical change in the ion transport mode, when the energy of electrostatic interaction between ions begins to significantly exceed the energy of their thermal movement ($k_B T$).

As mentioned above, another important parameter affecting the ion current is dynamic viscosity η of the solvent. An increase in viscosity in the water confinement conditions leads to a decrease in convective flow (electro-osmotic flow) (see equations (1) and (6)), as well as to a decrease in the ion diffusion coefficient according to the Stokes–Einstein equation:

$$D = \frac{k_B T}{6\pi\eta a}, \tag{11}$$

where a is the effective ion radius. Thus, when η increases by a factor of 5 – 10 under confinement, diffusion is proportionally reduced. In equation (6), the value of the kinematic viscosity μ is used. The dynamic and kinematic viscosities are related by the following expression $\mu = \eta/\rho$, where ρ is the density of the medium (kg/m^3).

Figures 3(a, dashed curve 2) and Fig. 3(b, dashed curve 2) present the approach curves $I(z)$ calculated using the modified PNP-NS model that incorporates nanoscale confinement effects. Fig. 5 further illustrates model curves at negative pipette bias for different surface charge densities on the sample.

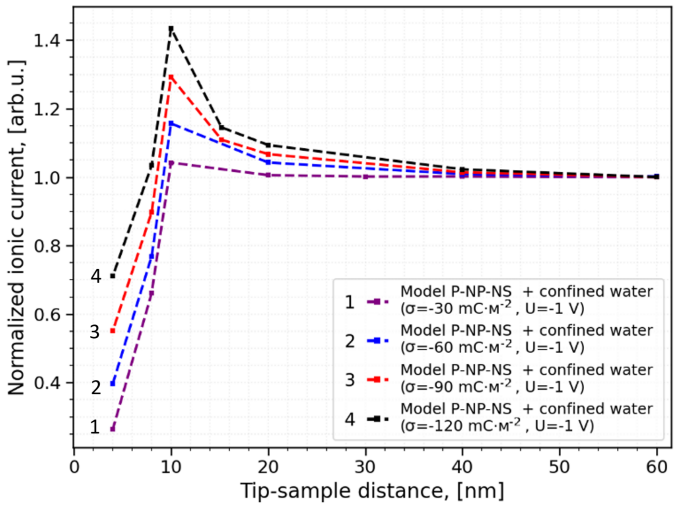

FIG. 5. Theoretical approach curves $I(z)$ with negative voltage bias $U = 1$ V on the electrode in the NP, obtained for different sample surface charges densities σ. NP's surface charge density for all modeled cases was $\sigma_{pip} = -30$ mC·m^{-2}

4. Discussion

When comparing experimental and simulated approach curves $I(z)$, it is important to properly define the probe-sample separation. In the model, the gap is an explicit parameter; in SICM, however, it is not measured directly. Instead, the extension of the piezo scanner is monitored until the ionic current decreases to its minimum detectable value.

In an ideal case with perfectly rigid probes and samples, atomically smooth and parallel surfaces the scanner extension would equal the true distance between the pipette and the sample. The minimum current would then be limited by instrumental noise only. In practice, however, the situation is more complex. On soft surfaces (e.g., polymers or living cells), electroosmotic pressure [34] and Coulombic repulsion between like charges on the pipette and sample can deform the surface, effectively increasing the gap. This introduces systematic errors in estimating the true probe-sample distance from piezo extension. Additional factors such as surface roughness and imperfect parallel alignment also affect the residual current at contact, further complicating tip-sample distance determination.

For this reason, in our analysis we restrict quantitative comparison between experiment and theory to hard, smooth samples (e.g., polystyrene), where errors in gap determination are minimal (Fig. 3(a,b), solid curves 2).

In the conventional interpretation of "no-peak" approach curves in SICM, current decay is attributed to the increasing total resistance, consisting of contributions from the nanopipette interior, the gap, and the bulk electrolyte [24]. In such cases, the descending branch of $I(z)$ is well reproduced both by Ohmic theory (Fig. 3(a, dashed curve 4)) and the classical PNP-NS model (Fig. 3(a, dashed curve 3)). However, comparison with experimental data (Fig. 3(a, solid curve 1)) shows clear discrepancies in the onset of current decay. This indicates that both Ohmic and classical PNP-NS models become inaccurate at nanoscale separations. By contrast, the modified PNP-NS model that includes surface charge and nanoscale water confinement effects (Fig. 3(a, dashed curve 2)) shows significantly improved agreement with experiment.

The sign and magnitude of surface charge on dielectric materials in aqueous media are typically determined by silanol group dissociation or anion adsorption, with glass and most polymers acquiring negative charge at pH greater than 4. In our modeling, surface charge density served as a fitting parameter. The surface charge density of polystyrene extracted from our approach curves was approximately twice the value obtained using a macroscopic surface tension method [35]. We attribute this discrepancy to the different sampling scales: the droplet-deflection method averages over $\sim$1 mm^2, whereas SICM provides highly localized measurements ($\sim 10^{-8}$ mm^2), which can differ from the mean surface charge density value.

A more pronounced divergence between experiment and theory arises under negative pipette bias, when current enhancement due to surface charge is observed. In principle, such enhancement can occur at both positively and negatively charged surfaces. For negatively charged materials such as glass, many polymers, and chromosomes in physiological

solutions [16], the growth branch appears at negative pipette potentials. For positively charged surfaces (e.g., APTES-modified or poly-L-lysine-treated glass), enhancement occurs at positive bias [15, 36].

In our experiments with polymer samples, the appearance of a peak was probabilistic ($\sim$60 %). We attribute this to surface heterogeneity, arising from local roughness and random distribution of functional groups. To test this hypothesis, we prepared glass samples with more uniform surface by etching in NaOH at 250 °C. On these surfaces, the peak effect was consistently observed ($\sim$100 %). However, we did not compare these data directly with simulations, since deformation and roughening of the etched glass surface must be considered. Indeed, Fig.2 shows that the effective tip-sample separation for etched glass is more than twice that for polystyrene (Fig. 3, solid curve 1). This indicates surface softening after alkali etching, consistent with sample deformation effects when decreasing the gap.

As emphasized earlier, the current growth branch of $I(z)$ has been extensively studied as a function of surface charge, pH, electrolyte concentration, and pipette aperture. However, all previous models predict monotonic growth up to zero gap (Fig. 3(b, curve 3)), and cannot reproduce the experimentally observed peak. Our model, which incorporates surface charge, reduced permittivity, and increased viscosity under nanoscale confinement, explains the origin of the peak. Specifically, confined water conditions halt the unbounded current growth otherwise predicted for a negatively biased glass pipette approaching a negatively charged surface.

The small offset ($\sim$10 nm) between the experimental and simulated peaks can be explained by the finite stiffness and roughness of polystyrene [37] and by slight misalignment between the pipette and the sample surface. Fig. 5 further illustrates that peak height is sensitive to sample surface charge density, highlighting the potential of SICM as a nanoscale probing method of local surface charge of living cells.

Finally, the presence of a peak in $I(z)$ has practical implications for SICM operation. In standard feedback mode, the set-point is typically chosen at 99 % of I_{sat}. In the presence of a peak, however, this working point lies on the much steeper descending branch of $I(z)$ (Fig. 2(b)) compared to a no-peak curve (Fig. 2(a)). As a result, SICM images acquired under peak-effect conditions (Fig. 2(d)) exhibit increased noise relative to images obtained at positive bias without a peak (Fig. 2(c)). Thus, while the peak effect can serve as a useful tool for local surface charge detection and measurements, it must also be considered to ensure stable feedback operation.

References

[1] Hansma P.K., Drake B., Marti O., Gould S.A., Prater C.B. The scanning ion-conductance microscope. *Science*, 1989, **243** (4891), P. 641–643.

[2] Korchev Y.E., Bashford C.L., Milovanovic M., Vodyanoy I., Lab M.J. Scanning ion conductance microscopy of living cells. *Biophys. J.*, 1997, **73** (2), P. 653–658.

[3] Klenerman D., Korchev Y.E., Davis S.J. Imaging and characterisation of the surface of live cells. *Curr. Opin. Chem. Biol.*, 2011, **15** (5), P. 696–703.

[4] Rheinlaender J., Geisse N.A., Proksch R., Schäffer T.E. Comparison of scanning ion conductance microscopy with atomic force microscopy for cell imaging. *Langmuir*, 2011, **27** (2), P. 697–704.

[5] Pleskova S.N., Bezrukova N.A., Gorshkova E.N., Bobyk S.Z., Lazarenko E.V. A study of EA.hy926 endothelial cells using atomic force and scanning ion conductance microscopy. *Cell Tissue Biol.*, 2024, **18** (1), P. 36–44.

[6] Gorelik J., Shevchuk A., Ramalho M., Elliott M., Lei C., Higgins C.F., et al. Scanning surface confocal microscopy for simultaneous topographical and fluorescence imaging: application to single virus-like particle entry into a cell. *Proc. Natl. Acad. Sci. U.S.A.*, 2002, **99** (25), P. 16018–16023.

[7] Gu C., et al. Scanning ion conductance microscopy of living renal epithelial cells. *Kidney Int.*, 2002, **61** (3), P. 1250–1255.

[8] Shevchuk A.I., et al. Imaging proteins in membranes of living cells by high-resolution scanning ion conductance microscopy. *Angew. Chem. Int. Ed.*, 2006, **45** (14), P. 2212–2216.

[9] Muhammed Y., De Sabatino M., Lazenby R.A. The heterogeneity in the response of A549 cells to toyocamycin observed using hopping scanning ion conductance microscopy. *J. Phys. Chem. B*, 2025, **129** (20), P. 4904–4916.

[10] Pastre D., Iwamoto H., Liu J., Szabo G., Shao Z. Characterization of AC mode scanning ion-conductance microscopy. *Ultramicroscopy*, 2001, **90**, P. 13–19.

[11] Novak P., Li C., Shevchuk A.I., Stepanyan R., Caldwell M., Hughes S., et al. Nanoscale live-cell imaging using hopping probe ion conductance microscopy. *Nat. Methods*, 2009, **6** (4), P. 279–281.

[12] Page A., Perry D., Unwin P.R. Multifunctional scanning ion conductance microscopy. *Proc. R. Soc. A.*, 2017, **473**, 20160889.

[13] Wang X.-F., Duan Y.-F., Zhu Y.-Q., Liu Z.-J., Wu Y.-C., Liu T.-H., Zhang L., Wei J.-F., Liu G.-C. An insulin-modified pH-responsive nanopipette based on ion current rectification. *Sensors*, 2024, **24** (13), 4264.

[14] Yingfei M., Rujia L., Xiaoyue S., Dengchao W. Quantification of asymmetric ion transport in glass nanopipettes near charged substrates. *ChemElectroChem*, 2021, **8**, 3917.

[15] Clarke R.W., Zhukov A., Richards O., Johnson N., Ostanin V., Klenerman D. Pipette–surface interaction: current enhancement and intrinsic force. *J. Am. Chem. Soc.*, 2013, **135**, 322.

[16] Ushiki T., Ishizaki K., Mizutani Y., Nakajima M., Iwata F. Scanning ion conductance microscopy of isolated metaphase chromosomes in a liquid environment. *Chromosome Res.*, 2021, **29** (1), P. 95–106.

[17] Sa N., Lan W.J., Shi W., Baker L.A. Rectification of ion current in nanopipettes by external substrates. *ACS Nano*, 2013, **7**, 272.

[18] McKelvey K., Kinnear S.L., Perry D., Momotenko D., Unwin P.R. Surface charge mapping with a nanopipette. *J. Am. Chem. Soc.*, 2014, **136**, 13.

[19] Lukashenko S.Yu., Gorbenko O.M., Felshtyn M.L., Sapozhnikov I.D., Kirilenko D.A., Stepan V.P., Zhukov M.V., Golubok A.O. Ionic conductivity in nanopipettes: experiment and model. *Nanosyst.: Phys. Chem. Math.*, 2025, **16** (4), P. 441–449.

[20] Tao D., Jiang L., Jin M. A method of preparation of Ag/AgCl chloride selective electrode. *J. Wuhan Univ. Technol., Mater. Sci. Ed.*, 2018, **33**, P. 767–771.

[21] Cervera J., Schiedt B., Ramirez P. A Poisson/Nernst-Planck model for ionic transport through synthetic conical nanopores. *Europhys. Lett.*, 2005, **71**, 35.

[22] Apel P., Korchev Y.E., Siwy Z., Spohr R., Yoshida M. Diode-like single-ion track membrane prepared by electro-stopping. *Nucl. Instrum. Methods Phys. Res., Sect. B.*, 2001, **184**, 337.

[23] Rabinowitz J., Edwards M.A., Whittier E., Jayant K., Shepard K.L. Nanoscale fluid vortices and nonlinear electroosmotic flow drive ion current rectification in the presence of concentration gradients. *J. Phys. Chem. A*, 2019, **123** (38), P. 8285–8293.
[24] Nitz H., Kamp J., Fuchs H. A combined scanning ion-conductance and shear-force microscope. *Probe Microsc.*, 1998, **1**, P. 187–200.
[25] Laurance N. Self-diffusion of the chlorine ion in sodium chloride. *Phys. Rev.*, 1960, **120**, P. 57–62.
[26] Álvarez-Quintana S., Carmona F.J., Palacio L., Hernández A., Prádanos P. Water viscosity in confined nanoporous media and flow through nanofiltration membranes. *Microporous Mesoporous Mater.*, 2020, **300**, 110176.
[27] Bowen W.R., Welfoot J.S. Modelling the performance of membrane nanofiltration—critical assessment and model development. *Chem. Eng. Sci.*, 2002, **57**, P. 1121–1137.
[28] Wesolowska K., Koter S., Bodzek M. Modelling of nanofiltration in softening water. *Desalination*, 2004, **162**, P. 137–151.
[29] Deißenbeck F., Freysoldt C., Todorova M., Neugebauer J., Wippermann S. Dielectric properties of nanoconfined water: a canonical thermopotentiostat approach. *Phys. Rev. Lett.*, 2021, **126** (13), 136803.
[30] Fumagalli L., Esfandiar A., Fabregas R., Hu S., Ares P., Janardanan A., Yang Q., Radha B., Taniguchi T., Watanabe K., Gomila G., Novoselov K.S., Geim A.K. Anomalously low dielectric constant of confined water. *Science*, 2018, **360** (6395), P. 1339–1342.
[31] Girault H.H. *Analytical and Physical Electrochemistry*. EPFL Press: New York, 2004.
[32] Perry D., Momotenko D., Lazenby R.A., Kang M., Unwin P.R. Characterization of nanopipettes. *Anal. Chem.*, 2016, **88**, P. 5523–5530.
[33] Wright M.R. *An Introduction to Aqueous Electrolyte Solutions*. John Wiley & Sons: Chichester, UK, 2007.
[34] Kolmogorov V.S., Erofeev A.S., Woodcock E., Efremov Y.M., Iakovlev A.P., Savin N.A., et al. Mapping mechanical properties of living cells at nanoscale using intrinsic nanopipette–sample force interactions. *Nanoscale*, 2021, **13** (13), P. 6558–6568.
[35] Amadu M., Miadonye A. Determination of the point of zero charge pH of borosilicate glass surface using capillary imbibition method. *Int. J. Chem.*, 2017, **9**, P. 67–84.
[36] Perry D., Al Botros R., Momotenko D., Kinnear S.L., Unwin P.R. Simultaneous nanoscale surface charge and topographical mapping. *ACS Nano*, 2015, **9**, P. 7266–7276.
[37] Meyers G.F., DeKoven B.M., Seitz J.T. Is the molecular surface of polystyrene really glassy? *Langmuir*, 1992, **8** (9), P. 2330–2335.

Submitted 1 October 2025; revised 29 October 2025; accepted 30 October 2025

Information about the authors:

Stanislav Yu. Lukashenko – Institute for Analytical Instrumentation of the Russian Academy of Sciences, Russia; ORCID 0000-0002-5356-1261; lukashenko13@mail.ru

Olga M. Gorbenko – Institute for Analytical Instrumentation of the Russian Academy of Sciences, Russia; ORCID 0000-0002-7054-6602; gorolga64@gmail.com

Mikhail L. Felshtyn – Institute for Analytical Instrumentation of the Russian Academy of Sciences, Russia; ORCID 0000-0001-8677-061X; mfelsztyn@yandex.ru

Ivan D. Sapozhnikov – Institute for Analytical Instrumentation of the Russian Academy of Sciences, Russia; ORCID 0000-0003-2575-5015; isapojnikov@gmail.com

Stepan V. Pichakhchi – Institute for Analytical Instrumentation of the Russian Academy of Sciences, Russia; ORCID 0000-0002-8578-5200; pichakhchi.s@yandex.ru

Mikhail V. Zhukov – Institute for Analytical Instrumentation of the Russian Academy of Sciences, Russia; ORCID 0000-0003-3361-6947; cloudjyk@yandex.ru

Alexander O. Golubok – Institute for Analytical Instrumentation of the Russian Academy of Sciences, Russia; ORCID 0000-0001-9970-9172; aogolubok@mail.ru

Conflict of interest: the authors declare no conflict of interest.